Bioconjugate Chemistry

pubs.acs.org/bc

Article

Gene Regulation Using Nanodiscs Modified with HIF-1-α Antisense Oligonucleotides

Radhika Sharma, Yixiao Dong, Yuesong Hu, Victor Pui-Yan Ma, and Khalid Salaita*

Cite This: https://doi.org/10.1021/acs.bioconjchem.1c00505

Read Online

ACCESS | Metrics & More | Article Recommendations | Supporting Information

ABSTRACT: Delivery of nucleic acids can be hindered by multiple factors including nuclease susceptibility, endosome trapping, and clearance. Multiple nanotechnology scaffolds have offered promising solutions, and among these, lipid-based systems are advantageous because of their high biocompatibility and low toxicity. However, many lipid nanoparticle systems still have issues regarding stability, rapid clearance, and cargo leakage. Herein, we demonstrate the use of a synthetic nanodisc (ND) scaffold functionalized with an anti-HIF-1-α antisense oligonucleotide (ASO) to reduce HIF-1-α mRNA transcript levels. We prepared ND conjugates by using a mixture of phosphoglycerolipids with phosphocholine and phosphothioethanol headgroups that self-assemble into a ∼13 × 5 nm discoidal structure upon addition of a 22-amino-acid ApoA1 mimetic peptide. Optimized reaction conditions yield 15 copies of the anti-HIF-1-α ASO DNA covalently conjugated to the thiolated phospholipids using maleimide−thiol chemistry. We show that DNA-ND conjugates are active, nuclease resistant, and rapidly internalized into cells to regulate HIF-1-α mRNA levels without the use of transfection agents. DNA-ND uptake is partially mediated through Scavenger Receptor B1 and the ND conjugates show enhanced knockdown of HIF-1-α compared to that of the soluble ASOs in multiple cell lines. Our results demonstrate that covalently functionalized NDs may offer an improved platform for ASO therapeutics.

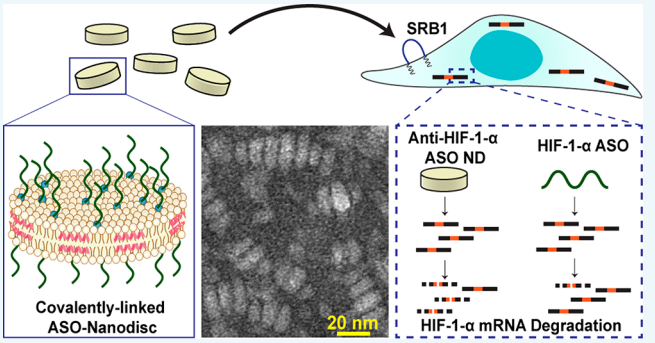

INTRODUCTION

Nucleic acid therapeutics have evolved into a highly attractive class of drugs that directly target the genetic basis for disease. One important type of nucleic acid drug is antisense oligonucleotides (ASO) typically comprising <20mer DNA or RNA nucleotides complementary to a target mRNA. There are currently eight FDA-approved ASO drugs, and a significant number are in clinical testing and early stage development.[1] Despite this progress, ASO drugs have met setbacks in the clinic, in part, because of two main challenges. The first pertains to the short half-life of these molecules due to the activity of endogenous nucleases.[2,3] The second major challenge is the highly charged backbone of DNA and RNA polymers that limits penetration across the plasma membrane.[4] To reduce nuclease susceptibility, the phosphate backbone is typically modified with a phosphorothioate (PS) or methyl modifications, while the ribose is often modified with 2′ methoxy or fluoro groups, as well as 2′−4′ cross-links.[5,6] These modified oligos underlie the most recently FDA approved ASO drugs. Inadvertently, the PS modification also leads to protein interactions, which results in increased cellular uptake for particular tissues.[7−9] Nonetheless, less than 1% of internalized DNA/RNA drugs reach the cytoplasm of the cell, and most are destroyed or trapped within endosomes.[10,11] Accordingly, any slight improvement in the delivery or stability of nucleic acid drugs will likely have a profound impact on the clinical application of such drugs. Indeed, thrombocytopenia, the depletion of platelets, is a common adverse event associated with the elevated dosing that is needed to achieve efficacy for ASO drugs.[12] Hence, improving the delivery and nuclease resistance of ASOs will enhance efficacy, thus reducing costs, and facilitating clinical adoption.

One general approach to addressing these challenges is using nanoparticle scaffolds which can assist in cellular penetration as shown by Mirkin and others.[13−15] Specifically, spherical nucleic acids (SNAs) ranging in size from 5 to 20 nm are ideally suited for delivery, because they escape clearance mechanisms and enhance cell uptake as shown in prior work.[16,17] Lipid-based nanomaterials are especially attractive because phospholipids offer high biocompatibility with facile and simple synthetic preparation techniques and minimal toxicity, in comparison to inorganic scaffolds, such as metal

Received: October 26, 2021
Revised: December 16, 2021

Scheme 1. Protocol for Preparing and Assembling DNA-ND Conjugates[a]

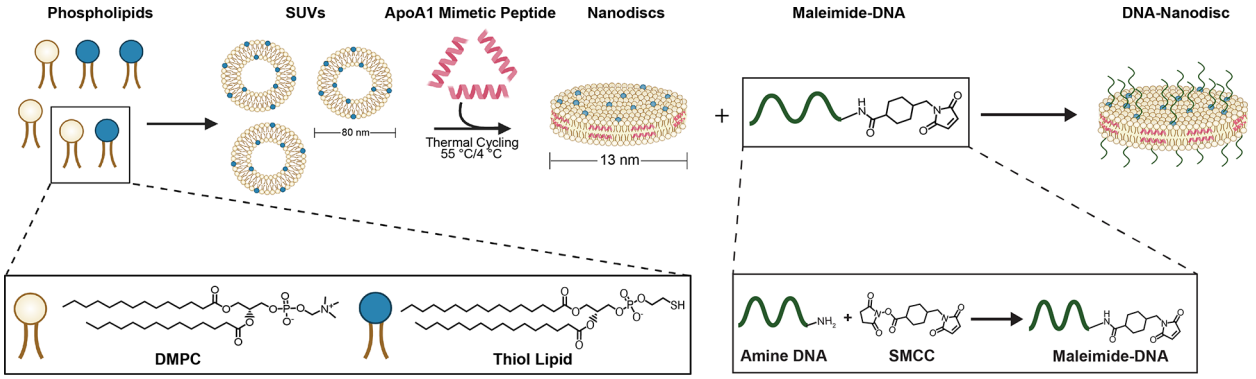

[a]NDs are formed by preparing 80 nm small unilamellar vesicles (SUVs) primarily using DMPC as a major component and the thiol phospholipid as a minor component (~10%). A short 22-amino-acid peptide ApoA1 mimetic is added to SUVs before subjecting them to thermal cycling between 55 °C and 4 °C to form NDs. DNA bearing a maleimide group is chemically conjugated to the thiol NDs resulting in the DNA-ND conjugate. The product is purified by using size exclusion chromatography.

nanoparticles. Phospholipids will spontaneously self-assemble into liposomes, which are the most commonly investigated class of lipid nanoparticles for delivery. However, liposomes typically range from 30 nm to 2.5 μm in diameter, which leads to some level of clearance *in vivo*, and are best suited to encapsulate materials within their aqueous cavity. To enhance delivery, an ideal nanomaterial would be one that is small, ideally 10−60 nm[18] in size, highly monodisperse, stable, and biocompatible.

Nascent high-density lipoprotein (HDLs) particles are well suited for delivery given their size, which is typically ~10 nm in diameter with a thickness of ~5 nm. HDLs are naturally occurring and play a prominent role in delivering cholesterol to the liver through reverse cholesterol transport. In addition to cholesterol transport, HDL is commonly referred to as a multivalent particle because of its inherent role in transporting and delivering various molecular cargo including nucleic acids (miRNAs) through its non-endocytic mechanism of Scavenger Receptor B1 (SRB1) delivery,[19] thus highlighting its natural role as a delivery vehicle. While the nascent HDL particles are composed of ApoA1, phospholipids, and several other minority component proteins, the structure of HDLs can be easily recapitulated using specific phospholipids and short ApoA1-mimetic peptides,[20,21] herein referred to as synthetic nanodiscs (NDs). The advantages of using NDs for delivery include a facile and scalable synthesis, biocompatible composition, and evasion of clearance because of their sub-20 nm size. Additionally, NDs can also transfer their content directly into the cytoplasm of a cell via SRB1, bypassing endosomal entrapment.[22] SRB1 is commonly expressed in many cellular subtypes, hence widening the realm of possibilities for targeted delivery. Furthermore, nonspherical nanoparticles such as NDs may also offer a lower energetic barrier for internalization,[23] thus enhancing cell delivery. Therapeutic oligonucleotides, such as siRNA,[24−29] DNA,[15,21,30] PNA,[31] and miRNA,[32] are typically anchored onto NDs using noncovalent linking strategies through cholesterol tagging[15,22,25,33] or electrostatic attraction[31,32,34,35] using NDs assembled with positively charged phospholipids or polylysine. One of the challenges in using ND for oligonucleotide delivery pertains to the labile nature of these interactions, which leads to instability of the conjugates. For example, the observable k_{off} between cholesterol-labeled oligonucleotides and phospholipid membranes is reported as ~10^{-2} to 10^{-3}/s (ref 36) and hence offers short half-lives, $t_{1/2}$ of ~1−10 min. Another problem with the noncovalent assembly of ND−nucleic acid conjugates is the low density of oligonucleotides, which has been optimally reported as ~1−8 oligonucleotides per ND.[25,37,38] It is thus desirable to generate covalently linked ND−nucleic acid structures with greater densities of nucleic acids to boost their ASO activity.

Herein, we address these problems and generate covalently linked ASO-ND conjugates with the greatest reported density of DNA, to the best of our knowledge. Specifically, we tested a range of bioconjugation methods and identified the maleimide−thiol Michael addition chemistry as the most favorable. By titrating different thiol phospholipid concentrations and various reaction conditions (temperature and pH), we were able to boost the density of DNA to maximally 15 copies/ND while maintaining the NDs ultrasmall size and monodispersity. Importantly, we found that ND conjugation afforded enhanced nuclease resistance. As a proof-of-concept, we studied the uptake and efficacy of ND conjugated to a clinically relevant ASO that targets hypoxia inducible factor 1 alpha (HIF-1-α). We tested this particular ASO because it was evaluated in phase 1 dose escalation studies in patients with advanced solid tumors and showed no dose-limiting toxicities.[39,40] Our results show that ASO-NDs are taken up by a variety of cell types and internalization is SRB1-dependent. ASO-NDs are also highly active in knocking down HIF-1-α in a time- and concentration-dependent manner. On an ASO-basis, our ND-conjugation approach affords ~3-fold improvement in knockdown of HIF-1-α in HeLa cells (75 nM of the ASO, 24 h) when compared to the ASO itself, which represents a marked enhancement in drug efficacy. Overall, our work describes a facile and easily adaptable conjugation strategy for linking ASO drugs to NDs that may potentially enhance efficacy.

RESULTS AND DISCUSSION

Incorporating and Assembling Thiol-Functionalized NDs. NDs were prepared from small unilamellar vesicles (SUVs) comprised of 1,2-dimyristoyl-*sn*-glycero-3-phosphocholine (DMPC) and 1,2-dipalmitoyl-*sn*-glycero-3-phosphothioethanol (referred to as thiol lipid). To self-assemble the NDs from the SUVs (1 mL of lipid at 2.5 mg/mL), 751 nM of

https://doi.org/10.1021/acs.bioconjchem.1c00505
Bioconjugate Chem. XXXX, XXX, XXX−XXX

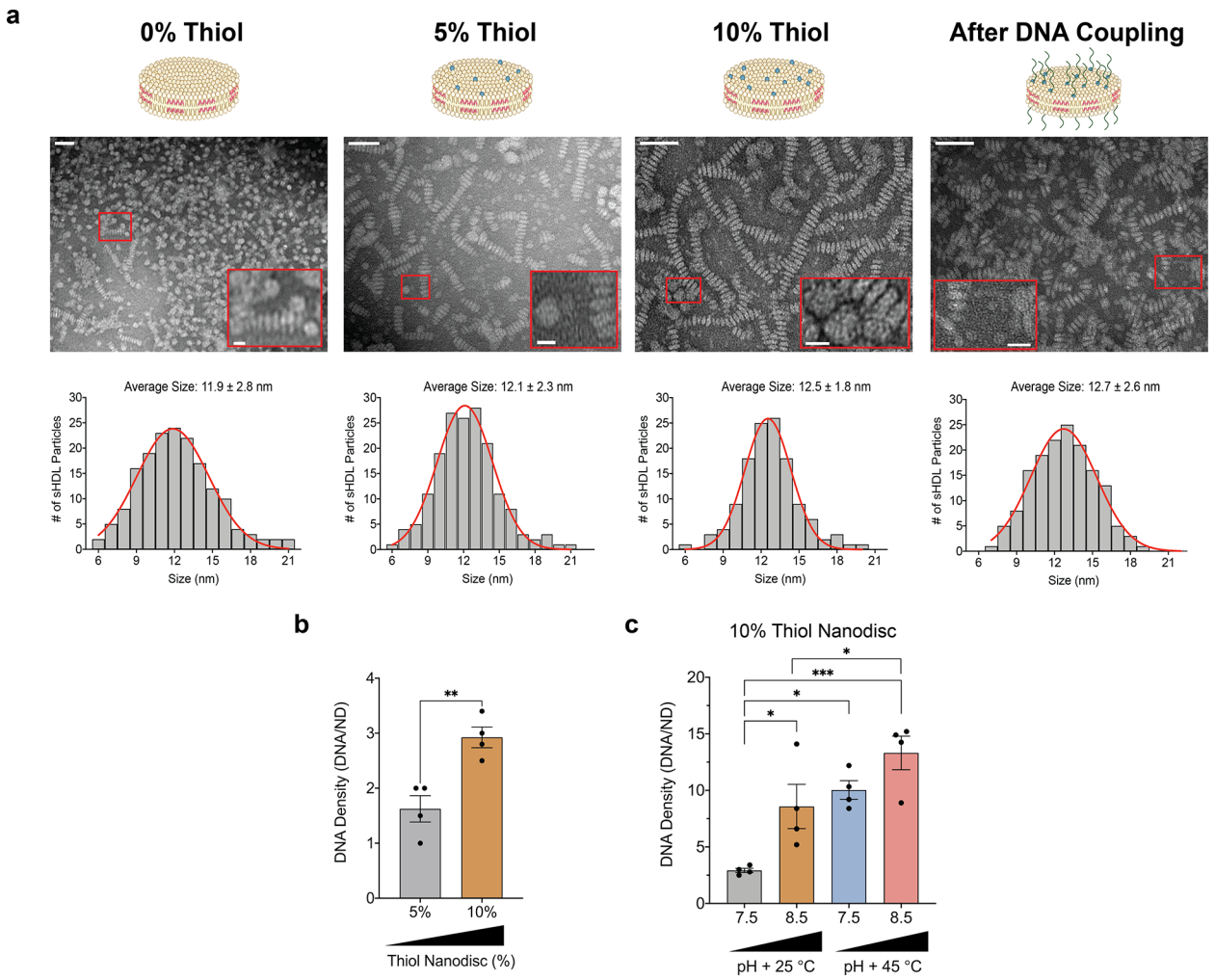

Figure 1. Coupling and optimizing DNA onto the ND surface. (a) TEM images (top) and binned size analysis (bottom, n = 170 NDs from 3 different images for each group) of NDs composed of DMPC only, 5% thiolated lipid, 10% thiolated lipid, and after DNA is coupled onto a 10% thiol ND surface. Scale bar: 50 nm; inset: 30 nm. Samples were prepared using a plasmon-etched 400-mesh copper grid, and staining was performed using Nano-W. Diameter differences between each ND group are not statistically significant. (b) Plot comparing DNA density of DNA-ND conjugates consisting of NDs with 5% thiol or 10% thiol. The 10% thiol ND shows a greater DNA density (3 DNA/ND vs 1.6 DNA/ND for 5%) at standard reaction conditions: 25 °C, pH 7.4. (c) Plot comparing the DNA density on 10% thiol ND after testing different pH (7.5 and 8.5) and temperature (25 °C and 45 °C) conditions. There is an average increase in DNA density from 3 ± 0.5 DNA/ND to 13 ± 2 DNA/ND under the improved conditions. Each data point represents one independent replicate. Error bars represent SEM of n = 4 independent replicates and * p < 0.05, ** p < 0.01, *** p < 0.001.

ApoA1-mimetic peptide (PVLDLFRELLNELLEALKQKLK) was incubated with the SUVs, and the samples were subjected to thermal cycling (Scheme 1). In preliminary experiments, we tested strain-promoted Cu-free click reactions to couple nucleic acids to NDs. However, these methods generated low DNA conjugation yields in our hands and were not pursued further (Figure S1). Instead, we found that coupling between maleimide-activated DNA to a thiolated ND produced the most promising initial yields. Therefore, we first aimed to optimize the coupling efficiency by determining the maximum density of the thiolated lipids that could be incorporated into the ND. We tested a range of molar percentages (5−20%) of thiol lipids and assessed the ND structure using transmission electron microscopy (TEM). We observed that 5 mol % and 10 mol % thiol-NDs (Figure 1a) displayed a monodisperse morphology, whereas the 20 mol % thiol-NDs showed aggregation and broadening of ND size (Figure S2). We postulate that the thiolated lipids can lead to the formation of disulfide bonds, prompting aggregation. Moreover, the thiolated lipids have a longer lipid tail which may contribute to the observed aggregation. Quantification of TEMs indicated that ND diameters slightly increased with increasing thiol lipid content (Figure 1a), though the values are not significant. For example, the 0% thiol ND had a diameter of 11.9 ± 2.8 nm, and this increased to 12.1 nm ± 2.3 nm for 5 mol % thiol ND, and 12.5 nm ± 1.8 nm for the 10 mol % thiol NDs. As expected, the ND thickness seemed independent of thiol concentration and was approximately 4.4, 4.5, and 4.7 nm for the 0%, 5%, and 10% thiol lipid ND particles respectively. Moreover, the ND thickness and diameter were consistent with the reported dimensions for DMPC bilayers and other NDs generated using different protocols,[41−45] confirming that the ND structures formed appropriately and likely adopted the structural beltlike conformation reported in other literature.[21] We were able to distinctly visualize the top and side views of NDs, and these distinct structural differences confirmed the disc-like configuration typical of nascent native HDL and NDs. We also observed ND "coin-like" stacks ascribed to the

https://doi.org/10.1021/acs.bioconjchem.1c00505
Bioconjugate Chem. XXXX, XXX, XXX−XXX

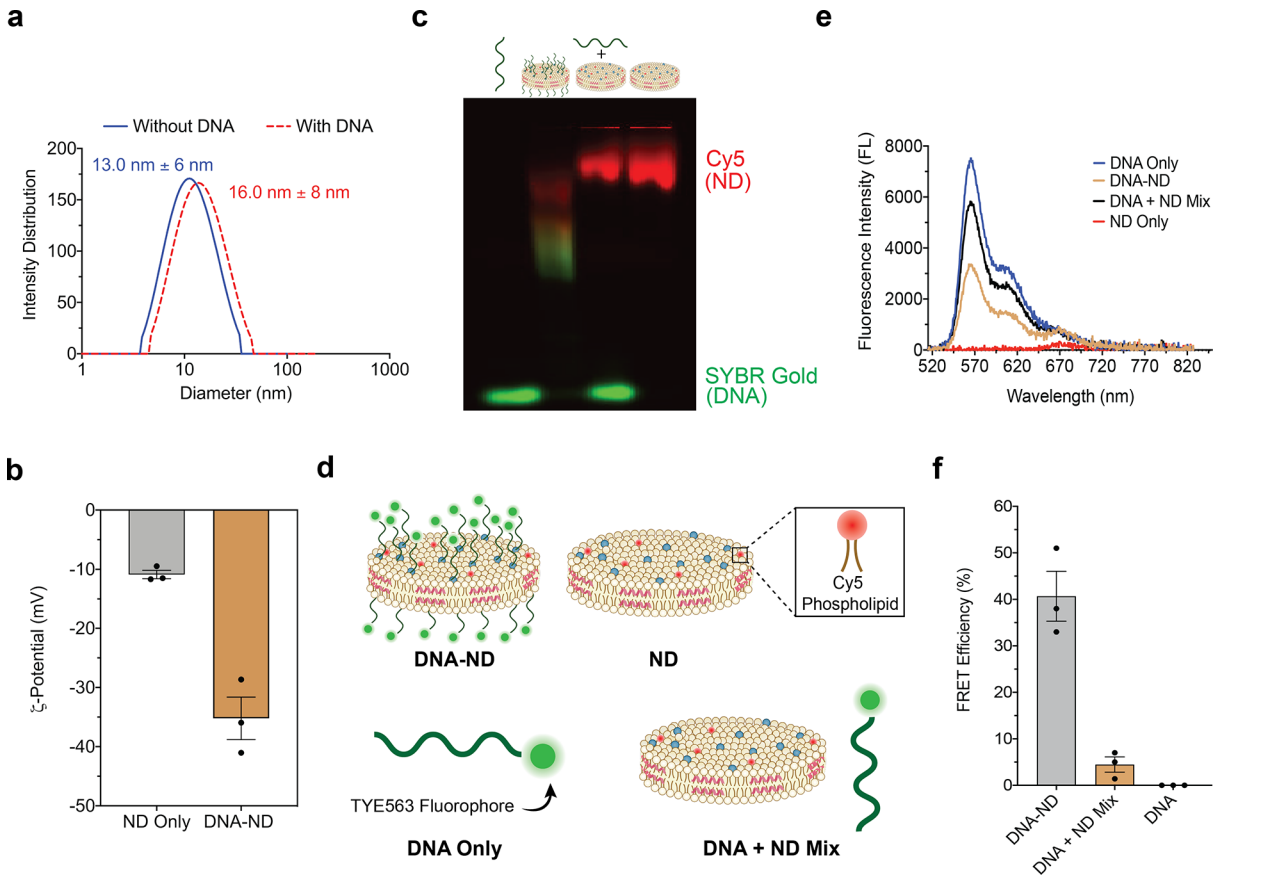

Figure 2. Validating and characterizing the attachment of DNA onto the surface of ND. (a) DLS graph indicating a shift in the hydrodynamic radius from 13.0 to 16.0 nm after conjugating DNA to the ND. Size distribution profile is a representative graph of a typical sample (n = 3 independent experiments) containing ND or ND with DNA conjugate. (b) Zeta-potential graph showing the increase in negative charge from −10.9 to −35.2 mV after DNA is coupled onto the surface of the ND. (c) Gel electrophoresis of four samples (L to R): DNA only, DNA coupled to ND, DNA mixed with ND, and ND only. NDs were prepared using a Cy5 phospholipid, and the gel was prepared using 1.5% agarose, in-gel staining using SYBR Gold and TAE buffer. The gel ran for 90 min at 85 V before imaging using a laser scanner. There is a retardation of DNA once attached to the ND compared to the unbound DNA lanes. (d) Schematic representation showing the different samples: DNA only, ND only, DNA-ND, and DNA mixed with NDs that were used for the FRET assay. TYE labeled DNA and Cy5 labeled phospholipid NDs were used for FRET. (e) Fluorescence spectra of the four groups illustrated in (d) when excited at λ = 520 nm. DNA was measured at a concentration of 100 nM, while 8 nM ND concentration was used to best match the ND and DNA + ND mix concentration in the DNA-ND sample. (f) Plot of the calculated FRET efficiency of the chemically conjugated DNA-NDs compared to the unlinked DNA and ND mixture. The higher FRET efficiency (40.1%) of the DNA-ND compared to the mixed control (4.5%) further substantiates that DNA is bound onto the surface of the ND. Each data point represents one independent replicate. Error bars represent SEM of n = 3.

"rouleaux effect", a common artifact of the negative staining process in TEM due to the interaction of the negatively charged particles in the stain with the choline headgroups during the drying process.[41,46]

ND Conjugation to DNA. In order to facilitate a maleimide−thiol linkage onto the surface of ND, an amine-terminal DNA was modified with a maleimide group bearing a heterobifunctional linker, succinimidyl 4-(*N*-maleimidomethyl)cyclohexane-1-carboxylate (SMCC). For our initial proof-of-concept studies, we chose to prepare DNA-ND conjugates by using a deoxyribozyme (DNAzyme) as a model nucleic acid which has catalytic activity that is highly sensitive to the local environment.[47] The maleimide-activated DNAzyme (DNA) was then coupled to the surface of NDs (Scheme 1) which were first treated with tris(2-carboxyethyl)phosphine (TCEP) to reduce the thiols. We measured the DNA density on NDs using the OliGreen assay (see Materials and Methods) and compared densities for NDs displaying 5 and 10 mol % thiol lipids under standard reaction conditions (RT, pH 7.4, 2 h). As expected, NDs composed of 10 mol % thiol lipids displayed a greater DNA density compared to the 5 mol % (Figure 1b). These results prompted us to optimize the coupling conditions (Figure 1c) by varying temperature (25 and 45 °C) and pH (7.4 and 8.5). Elevated temperatures in combination with a more basic pH resulted in an average DNA density (13 ± 2 DNA strands/ND). We did not increase the pH and temperature further to avoid disrupting the ND structure and activating lysines in the ND. Note that this coupling strategy and conditions resulted in DNA densities that significantly exceed that of cholesterol tagged siRNAs. We also confirmed through TEM that DNA modification and exposure to higher temperature and pH conditions did not alter the structure of the ND (Figure 1a), signifying that the structure-dependent properties of DNA-ND remain intact and still resemble that of discoidal pre-β HDL.

We next performed a set of experiments to validate DNA conjugation to the ND. DLS indicated a shift in the hydrodynamic radius after coupling with DNA (Figure 2a), and the average size of NDs increased from 13 nm ± 4 nm to 15 nm ± 7 nm (n = 3 independent replicates). ζ-Potential

https://doi.org/10.1021/acs.bioconjchem.1c00505
Bioconjugate Chem. XXXX, XXX, XXX−XXX

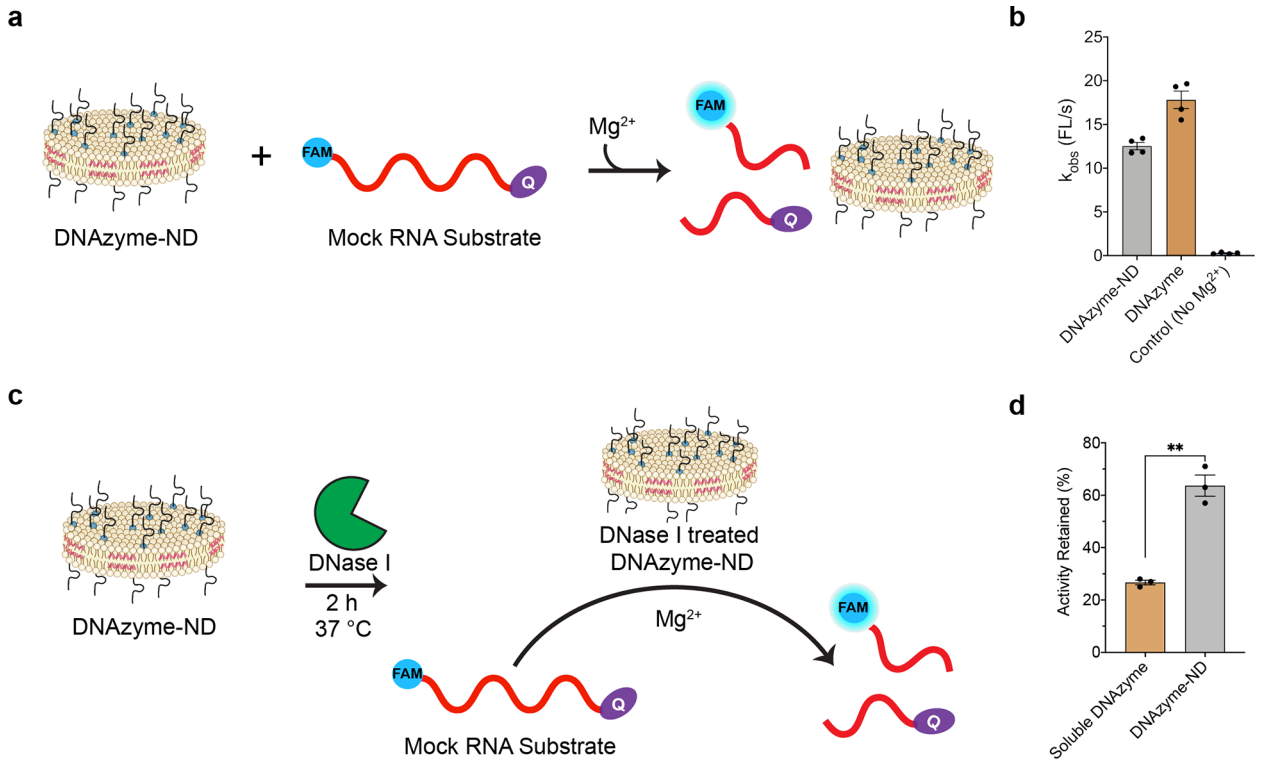

Figure 3. DNA conjugated to the surface of the ND is catalytically active and nuclease-resistant. (a) Scheme depicting the fluorescence assay used to assess catalytic activity using a DNAzyme-ND and a fluorogenic mock RNA substrate. Under the presence of Mg^{2+}, the DNAzyme will cleave the quenched substrate, leading to an increase in fluorescence. (b) Plot showing the difference in k_{obs} for the cleavage assay using the soluble DNAzyme, DNAzyme-ND, and a control with no magnesium in the buffer. The DNAzyme only group showed the highest cleavage rate, followed by DNAzyme-ND. Error bars represent SEM of $n = 4$. (c) Scheme showing the treatment of the DNAzyme-NDs with DNase I for 2 h prior to measuring catalytic activity using the fluorogenic mock RNA substrate. (d) Plot showing the relative activity retained after DNAzyme-ND conjugates, and soluble DNAzymes were treated with DNase I for 2 h at 1 U. The ND scaffold afforded greater protection against DNase I as it retained higher activity, 64%, compared to the soluble nucleic acid which only retained 27%. Each data point represents one independent replicate. Error bars represent SEM of $n = 3$ and ** $p < 0.01$.

measurements showed a drastic shift from −10.9 mV to −35.2 mV (Figure 2b) after DNA conjugation, indicating the presence of negatively charged nucleic acid on the surface of the ND. We also used agarose gel electrophoresis to confirm covalent conjugation of the DNA in samples that had Cy5-tagged lipids (Figure 2c). The ND-conjugated DNA showed a marked retardation in migration compared to soluble DNA. In contrast, the ND band migrated more rapidly as a result of DNA conjugation, which is consistent with an increase in charge density as a result of DNA conjugation. Notably, we did not observe any changes in the bands when DNA was mixed with the ND, indicating weak, if any, electrostatic interactions (Figure 2c). The smear-like pattern in the DNA-ND sample is likely due to a distribution of DNA densities on each ND as well as disruption of the ND as it migrates in the gel. DNA-ND conjugates are highly stable in solution for up to 3 weeks at 4 °C, as confirmed by DLS measurements (Figure S3). FRET measurements further confirmed direct DNA conjugation to the ND (Figure 2d). Here, we tagged the short anti-HIF-1-α ASO (Table S2) with a TYE563 donor fluorophore while the ND incorporated a Cy5 acceptor fluorophore. Donor emission spectra showed that DNA conjugation led to a significant reduction in donor emission intensity when compared to donor-only sample or samples that mixed the DNA with the ND (Figure 2e). The calculated FRET efficiency was 40% for the DNA-ND conjugate and 5% for the mixture of the DNA and ND (Figure 2f). The relatively moderate FRET efficiency is because the acceptor is not directly attached to the TYE-labeled DNA. Rather, the donor (TYE-DNA) and the acceptor (Cy5 phospholipids) are localized to the same ND, and thus the FRET efficiency reflects the statistically averaged donor−acceptor distance. Collectively, these results establish that the DNA is chemically linked to the ND, prompting us to next investigate the activity of the DNA-ND conjugates and their nuclease resistance.

DNA Bound to the Surface of the ND is Functional and Nuclease-Resistant. Recent work has shown improved therapeutic potential for DNAzymes further motivating these sets of experiments.[48,49] For our experiments, we used a novel DNAzyme sequence that has been identified in our lab. We measured the activity of the DNAzyme containing the catalytic loop derived from the 10−23 DNAzyme[14,47,50−52] against a fluorogenic substrate. To achieve multiple turnover kinetics, the kinetic measurements employed a 10-fold excess of the substrate compared to the DNAzyme-ND (or soluble DNAzyme). The nucleic acid substrate was dual-labeled with a FAM fluorophore at the 5′ terminus and an Iowa Black quencher at the 3′ terminus (Figure 3a). The FAM fluorescence intensity (FL) was monitored over a 4 h time period (Figure S4) and fits of these plots provided the k_{obs} rate constants. We found that DNAzyme-ND conjugates displayed ∼34% loss in activity compared to the soluble DNAzyme (Figure 3b) possibly due to sterics imposed by the ND surface.[53] Importantly, the ND afforded nuclease resistance, as

https://doi.org/10.1021/acs.bioconjchem.1c00505
Bioconjugate Chem. XXXX, XXX, XXX−XXX

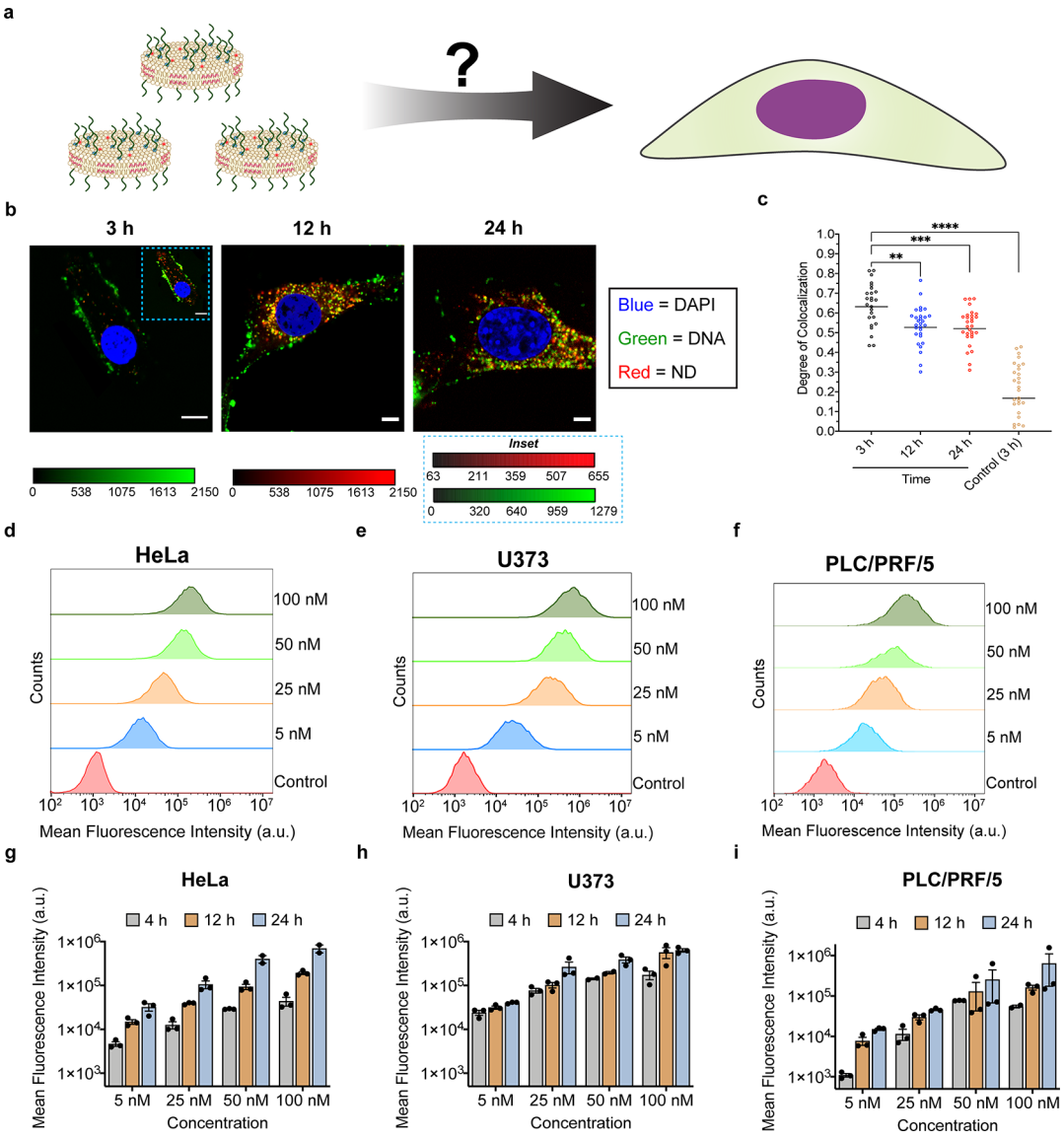

Figure 4. ASO-ND shows uptake into HeLa, U373, and PLC/PRF/5 cells in a dose- and time-dependent manner. (a) Scheme showing the possibility for ASO-ND to be internalized into cells. (b) Representative confocal microscopy images showing a time course for the uptake of 100 nM ASO-ND into HeLa cells. ASO was labeled with a TYE dye and the NDs were labeled with a Cy5 phospholipid. Cells were fixed and stained with DAPI before acquiring images with a 60× oil objective. Scale bar: 5 μm. (c) Pearson's colocalization coefficient analysis of TYE and Cy5 signal in n = 25−30 cells for each group. Analysis indicates the increased detachment of ASO from the ND within 12 h. Representative flow cytometry histograms at 12 h for (d) HeLa, (e) U373, and (f) PLC/PRF/5 cells that were treated with the indicated concentration of the ASO-ND and rinse prior to the measurement. Flow data represents intensities for a minimum of 5000 cells. Increase in uptake of ASO-ND over time measured at 4, 12, and 24 h as measured from the mean intensity from flow cytometry in (g) HeLa, (h) U373, and (i) PLC/PRF/5 cells. Each data point represents one independent replicate. Error bars represent SEM of n = 3 and ** $p < 0.01$, *** $p < 0.001$, **** $p < 0.0001$.

DNAzyme-ND conjugates retained 64% of their activity after treatment with DNase I for 2 h, while the soluble DNAzyme only preserved ∼27% of the activity after the same nuclease treatment (Figure 3c,d). Thus, the ND scaffold offers a suitable and robust candidate for delivery therapeutic nucleic acids. This is not surprising, as this structure resembles a nascent HDL scaffold that is known to offer protection against nucleases.[15] These results prompted us to investigate the uptake mechanisms and functional activity *in vitro*.

ASO-ND Conjugates Are Internalized in a Dose- and Time-Dependent Manner. For our *in vitro* studies, we transitioned toward using a clinically relevant ASO target as a test bed model to investigate the potential of ND conjugation in enhancing the function of validated ASOs. Our goal here was to quantify the uptake of ASO-ND conjugates using model cell lines (Figure 4a). We first incubated HeLa cells with ASO (anti-HIF-1-α ASO; see Table S2 for sequences used in this study) and phospholipid dual-tagged fluorescent ASO-ND conjugates for 3, 12, and 24 h. Then cells were washed and imaged by confocal microscopy (Figure 4b, Figure S5a). We observed accumulation of ASO and phospholipid scaffold inside the cytoplasm of the cells (Figure S5b) but were excluded from the nucleus. Importantly, ASO-ND conjugates were primarily localized to the cell edge at 3 h, indicating the cargo was associated with membrane and possibly trapped in early endosomes. The Pearson's coefficient for colocalization between the phospholipid and ASO was significantly higher than that measured for control samples containing a mixture of

https://doi.org/10.1021/acs.bioconjchem.1c00505
Bioconjugate Chem. XXXX, XXX, XXX−XXX

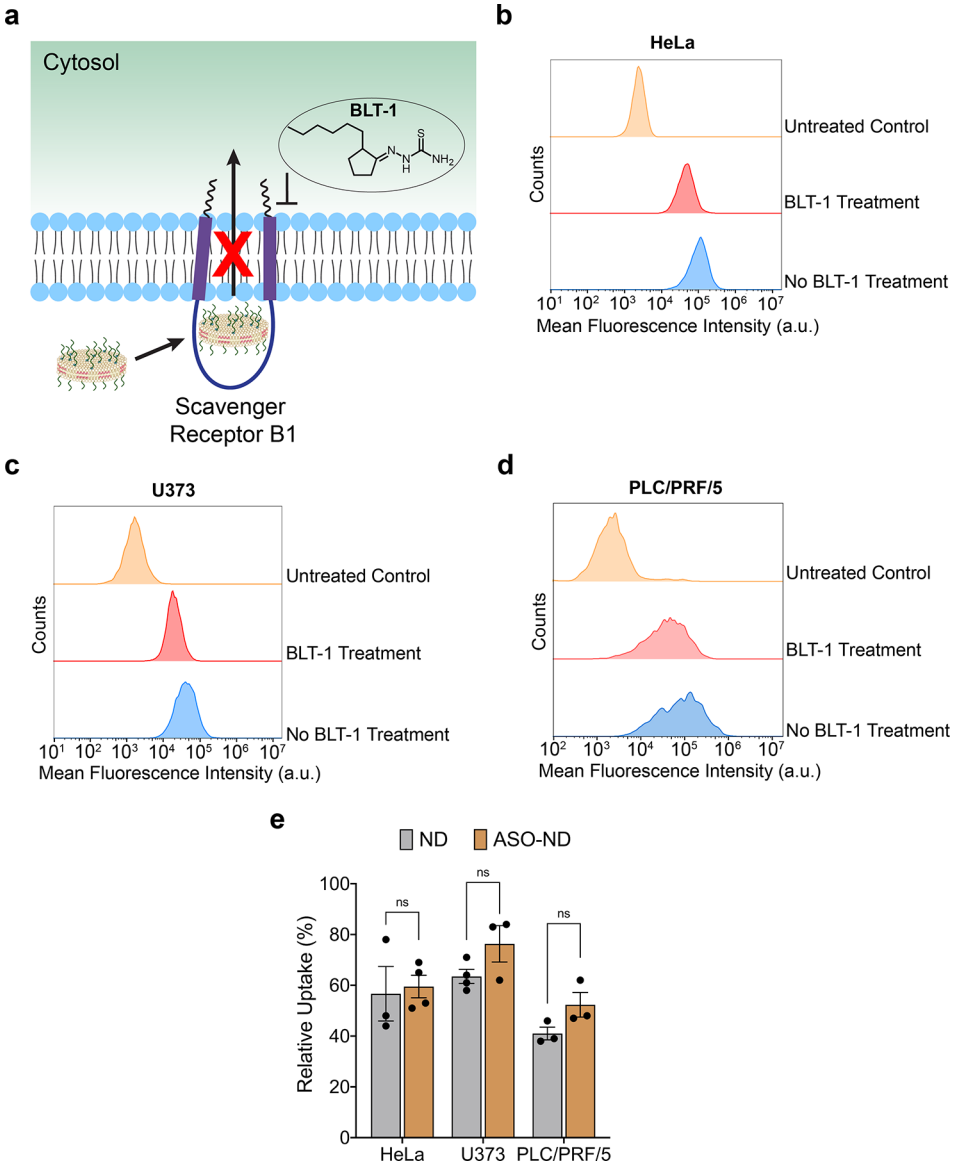

Figure 5. SRB1 partially mediates uptake of ASO-NDs in HeLa, U373, and PLC/PRF/5 cells. (a) Schematic showing the blocking of SRB1 on the cell surface with BLT-1 and how it can hinder the internalization of ASO-ND. Representative flow cytometry histograms measuring Cy5 intensity for cells that were pretreated with 50 μM BLT-1 for 1 h, and then incubated with the ASO-ND for 2 h in (b) HeLa, (c) U373, and (d) PLC/PRF/5 cells. The flow data reports mean intensities from a minimum of 5000 cells. (e) Graph comparing the uptake of ASO-ND or ND into cells after BLT-1 treatment. The values are normalized to the uptake level measured for the untreated control group. Representative flow cytometry histograms and plots of the ND only treated cells are shown in Figure S8 and Figure S9. Each data point represents the mean fluorescence intensity from an independent replicate. Error bars represent SEM of at least $n = 3$ replicates. There were no significant differences observed in the uptake after BLT-1 treatment for the ASO and ASO-ND groups.

NDs and ASO at all time points (Figure 4c). This shows that a significant subset of ASO-ND conjugates remain intact upon cell uptake. As expected, there is a decrease in colocalization at 24 h, indicating disassembly of the ASO-ND conjugates at later time points. We observe the presence of both ASO and ND puncta, which indicates that there are likely multiple populations of ASOs. Likely, a subset of ASOs are entrapped within endosomes, which would appear as puncta. Another population that appears as puncta is likely in the form of assembled phospholipid-ASO structures that have been internalized using the primary SRB1 uptake pathway for the NDs.[54] Additionally, because we used PS-modified ASOs, it is possible that the DNA was trafficked inside the cell using multiple productive and nonproductive entry pathways that would appear as puncta.[55] Since the DNA is lipidated, puncta may be associated with membranes such as the ER, nuclear membrane, mitochondrial membrane, plasma membrane, and other vesicle-like structures.[56]

We further investigated uptake of ASO-ND conjugates across multiple cell lines. Dose-dependent and time-dependent uptake into HeLa cells, U373 cells, and PLC/PRF/5 cells were quantified by incubating with fluorescently tagged ND and ASO-ND at varying concentrations (0−100 nM) for different lengths of time (4 h−24 h) prior to analyzing cells by flow cytometry. Both the scaffold (Figure S6) and the ASO-ND (Figure 4d−i) were taken up by the different cells in a similar dose- and time-dependent manner. It has been reported that NDs can be tolerated at higher doses, compared to other

https://doi.org/10.1021/acs.bioconjchem.1c00505
Bioconjugate Chem. XXXX, XXX, XXX−XXX

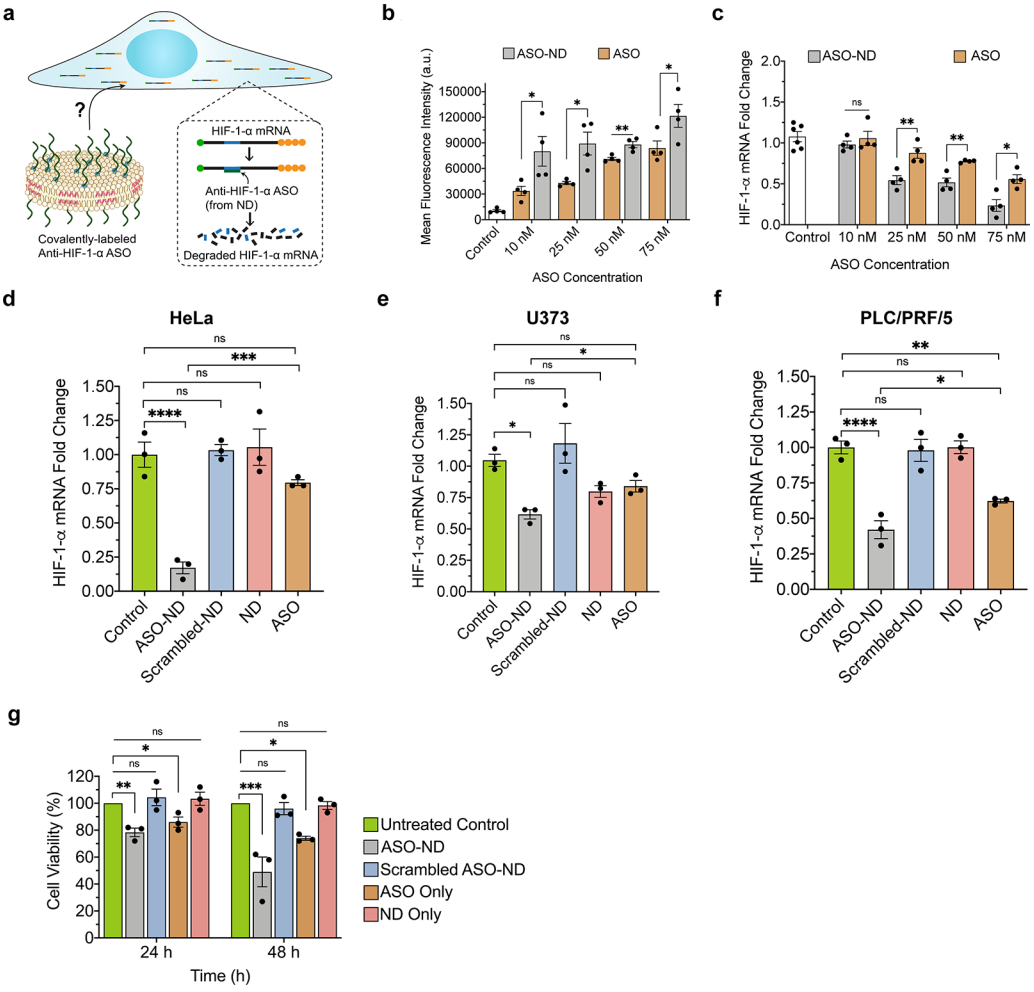

Figure 6. Quantifying the functional activity of ASO-NDs and ASOs that target HIF-1-α in three model cell lines. (a) Schematic showing the HIF-1-α transcript where the poly-A tail was denoted with orange circles, the blue represents that target region, and the 5′ capping was shown as a green circle. (b) Plot quantifying the uptake of ASO-ND (gray) and ASO (gold) in HeLa cells treated for 24 h as a function of ASO concentration. The ASO was tagged with a TYE dye and the mean fluorescence intensity per cell was determined using flow cytometry. Each data point represents one independent replicate. Error bars represent SEM of $n = 3$. (c) Plot comparing HIF-1-α levels in HeLa cells treated for 24 h with ASO and ASO-ND. Quantification was performed using RT-qPCR. Error bars represent SEM of $n = 4$, and all values were normalized to untreated control cells. (d–f) Plots of HIF-1-α levels determined by using RT-qPCR for HeLa, U373, and PLC/PRF/5 cells that were treated with 75 nM concentrations of ASO-ND, scrambled-ND, ND, and ASO for 24 h. The ASO concentration was matched at 75 nM in all groups; however, the ND group used a 7 nM concentration of ND. The transcript levels are normalized to the untreated control group. Error bars represent the SEM of $n = 3$. (g) Cell viability assessment in HeLa cells after dosing the HeLa cells with ASO-ND conjugates, ASO Only, Scrambled-ND, and ND only. Cell viability was assessed using MTT assay. HeLa cells were subjected to 75 nM ASO, and the ND group was subjected to 7 nM ND to best match ND concentration from the ASO-ND groups. The cells were incubated with sample for either 24 or 48 h before adding MTT reagent and performing the assay. The values are normalized to the OD measured at 590 nm for the untreated cells as a control. Each data point represents the percent viability for one independent replicate, and * $p < 0.05$, ** $p < 0.01$, *** $p < 0.001$, **** $p < 0.0001$.

nanoparticle scaffolds such as AuNPs and PEGylated liposomes.[57] Hence, at the ASO-ND concentrations tested, we do not observe saturation of uptake, suggesting that it may be possible to dose these conjugates at yet greater concentrations to further boost mRNA inhibition.

Uptake of Thiol NDs and ASO-NDs into Cells Is Partially Mediated by Scavenger Receptor B1. To elucidate the role of SRB1 in uptake, we performed RT-qPCR on HeLa, U373, and PLC/PRF/5 cells to confirm the expression of SRB1 (Figure S7). SRB1 levels were quantified relative to wild-type Huh7 cells, a known expressor for SRB1, as a positive control. The cell line panel was incubated with an inhibitor for SRB1 (Figure 5a), blocker of lipid transport-1 (BLT-1) before treatment with ND or ASO-ND for 2 h and measuring fluorescence intensity using flow cytometry. Fluorescence intensity of the inhibited cells were compared against cells that were treated with ASO-ND (Figure 5b–d) or ND (Figure S8) but no inhibitor. BLT-1-treated cells displayed reduced uptake compared to the cells treated with ND only, without BLT-1 (Figure S9). Notably, we observed that generally ASO-ND displayed more uptake compared to ND only (Figure 5e) after blocking the SRB1 receptor. This is likely due to the PS modifications, which mediate internalization through endocytosis by adsorption onto various cellular surface proteins, including SRB and LDL-receptor entry pathways.[9] Hence, the presence of PS modifications may further facilitate the trafficking of ASO-ND inside the cell, especially when conjugated to a delivery vehicle. We also noted that the uptake of ND and ASO-ND into PLC/PRF/5 liver cells was lower following BLT-1 treatment compared to the

https://doi.org/10.1021/acs.bioconjchem.1c00505
Bioconjugate Chem. XXXX, XXX, XXX−XXX

uptake in HeLa and U373 cells. This is not surprising, as hepatocytes are prominent expressors of SRB1 due to the inherent role of HDL docking and offloading of cholesterol for processing and clearance, and therefore these cells are more sensitive to SRB1 blocking.[58] Together, we conclude that the trafficking of thiol-NDs into cells is partially mediated by SRB1, a known pathway that circumvents endosomal entrapment by selectively taking up and delivering the ND content inside to the cytoplasm of the cells.

Anti-HIF-1-α ASO-ND Conjugates Are Active *in Vitro*. The transcription factor HIF-1-α is sensitive to hypoxia and aids in regulation of responses such as vascularization and angiogenesis that can ultimately tune oxygenation in tissues.[59] HIF-1-α also drives survival and adaptation to hypoxic or inflammatory conditions such as that found in solid tumors[60] and in wound healing.[61] Accordingly, there is significant interest in developing drugs that can downregulate the expression of HIF-1-α. Examples of HIF-1-α inhibitors include PX-478 and bortezomib, which are FDA-approved anticancer therapies. These inhibitors lack cell or tissue specificity and carry significant off-target effects,[62,63] thus prompting the development of nucleic acid-based drugs that target HIF-1-α at the transcript level. EZN-2968 is a potent HIF-1-α gapmer ASO that has undergone Phase I trial in patients with solid tumors and shown significant reduction of HIF-1-α levels in tumor biopsies.[39,40] Given the proven activity of this ASO, we aimed to evaluate the potency of anti-HIF-1-α ASOs upon conjugation to the ND phospholipids and to test whether function is maintained or potentially enhanced compared to the unmodified nucleic acid drug (Figure 6a).

First, we focused on HeLa cells and treated these cells for 24 h using different concentrations of ASO-ND and ASO. To best capture the potential activity of the ASO, no transfection agent was used in these experiments and the ASOs were spiked into the media at concentrations that ranged from 10 to 75 nM. We used a TYE-tagged ASO and ran flow cytometry to quantify the relative uptake levels. We generally observed dose-dependent internalization (Figure 6b) for both ASO and ASO-ND groups. ND-conjugation shows a significant increase in uptake compared to that of the unmodified ASO group. To test ASO function, we used identical conditions to those used for uptake measurements and then measured HIF-1-α levels using RT-qPCR (Figure 6c). We found a dose-dependent knockdown of HIF-1-α for both the ASO and ASO-ND group, in general agreement with the uptake data. Importantly, conjugation to the ND resulted in increased cellular internalization and increased reduction in HIF-1-α compared to the bare ASO. We normalized the knockdown levels by the uptake levels to estimate the effective activity of ASO when delivered in the unmodified and ND forms and found that the ND conjugation increased the potency of ASOs on a per molecule basis (Figure S9). In additional to enhanced nuclease resistance, another potential explanation for why ND conjugation leads to enhanced uptake and knockdown pertains to the internalization pathways for each type of ASO. For example, PS-modified ASOs can be routed to nonproductive pathways depending on the surface protein that internalizes the naked PS modified ASOs, resulting in dampened activity upon internalization.[55,64] In contrast, ND conjugation may lead to more productive pathways of uptake, such as HSPG and SRB1 mediated internalization, that allow the ASO to access the cytoplasm and the target mRNA.

To further validate this conclusion, we next treated the three cell lines: HeLa (Figure 6d), U373 (Figure 6e), and PLC/PRF/5 (Figure 6f) with ASO, ASO-ND, scrambled-ND, and ND for 24 h and measured HIF-1-α levels using RT-qPCR. These three cancer cell lines were selected because of their high intrinsic expression of HIF-1-α and their diverse source tissues. We maintained the ASO concentration in all groups to 75 nM with the exception of the ND group which lacked ASO, and hence we used 7.5 nM of the ND, thus best approximating the concentration of ND in the ASO-ND group. The ND group was included because of prior literature showing that certain ApoA1 mimetic peptides can downregulate HIF-1-α protein levels *in vitro* and *in vivo*,[65] but we did not detect modulation of HIF-1-α driven by the lipid nanoparticle platform. However, we found that the regulation of HIF-1-α was specific to the ASO, as we observed no knockdown with the scrambled sequence. The ASO-ND group showed greater levels of HIF-1-α knockdown when compared to the ASO only group across the three cell lines tested. We were surprised to find that SRB1 expression was poorly correlated with ASO-ND activity, as SRB1 expression followed this trend PLC/PRF/5 > U373 > HeLa (Figure S7) while ASO-ND knockdown efficiency followed this trend HeLa > PLC/PRF/5 > U373. Given that the uptake of NDs (Figure S6) and knockdown efficiency of the unconjugated ASOs was similar in all three cell lines (~25%) (Figure 6d–f); this suggests other mechanisms of enhanced uptake specifically for the ASO-ND conjugates in HeLa cells. Regardless of the differential levels of enhanced knockdown across the cell lines tested, delivery of ASOs using NDs is found to be highly advantageous for modulating gene expression levels *in vitro*.

HIF-1-α is important for cancer cell survival and proliferation, and its knockdown can reduce cell survival.[66] Therefore, we further confirmed the functional activity of the ASO by measuring cell viability (Figure 6g). In this experiment, HeLa cells were treated for 24 and 48 h, and then cell viability was measured using the MTT assay. We included 5 groups: ASO-ND, Scrambled ASO-ND, ND only, and ASO only. Across three independent experiments and at the 24 and 48 h time points, we observed the most significant decrease in cell viability for cells treated with the ASO-ND compared to untreated cells or to cells treated with scrambled ASO-ND. Interestingly, the soluble ASO also showed a decrease in cell viability at 24 and 48 h. These results are consistent with the HIF-1-α knockdown levels (Figure 6d) which showed that the ASO-ND was more active compared to the soluble ASO. In summary, we are able to achieve efficient delivery and functional activity of the ND-tethered HIF-1-α ASO at a greater level than that of the soluble ASO. Thus, this conjugation strategy may enable improved ASO delivery and enhanced therapeutic activity.

CONCLUSION

We developed a facile and efficient approach to generating nucleic acid–ND conjugates. NDs self-assemble from SUVs composed of 90% DMPC and 10% thiolated phospholipids after adding a 22-amino-acid ApoA1 mimetic peptide. DNA is covalently conjugated to the surface of the ND using thiol–maleimide coupling. TEM was used to determine the maximum thiolated phospholipid content that can be tolerated and thus help achieve NDs with up to 15 DNA copies per ND. Using this procedure, we showed that deoxyribozyme–ND conjugates are functional and are partially protected from

https://doi.org/10.1021/acs.bioconjchem.1c00505
Bioconjugate Chem. XXXX, XXX, XXX–XXX

DNase activity when compared to soluble oligonucleotides. ASO-ND conjugates are internalized by cells and show time and concentration dependent uptake. Dual-tagged ASO-ND conjugates display reduced colocalization as a function of time in cells and hence confirm separation of the ASO and phospholipid components over time. Using a small molecular inhibitor, we found that uptake is partially mediated by SRB1. ASO-ND conjugates selective for HIF-1-α showed greater activity than that of the soluble ASO drug, without the use of transfection agents, and across a panel of three cell lines. The enhanced activity is likely to due to nuclease resistance, enhanced uptake, and improved bypass of endosomal entrapment and potentially due to multivalency which may boost affinity to its target.[67] Importantly, ND can be engineered to deliver multiple cargos including miRNAs and siRNA as well as lipophilic molecules and peptides, and hence this platform may have broader applications as a therapeutic. Future work with ASO-NDs include expanded testing in other cell types, such as primary cells which may have different propensities for ND and ASO-ND uptake. More broadly, the *in vivo* activity of ASO-ND conjugates has also yet to be explored, as it remains unclear how these conjugates will distribute across different tissues and perform ASO function in animal models. That said, there is a physiological parallel for regulating HIF-1-α levels using oligonucleotide-linked HDL particles, as it was recently found that hypercholesterolemia leads to elevated expression of microRNA-126 loaded HDL particles which directly downregulate HIF-1-α levels in pig models.[68] In summary, this work describes the synthesis and characterization of an ASO-ND conjugate, and we look forward to developing this platform as a potential drug delivery system for cancer therapy.

MATERIALS AND METHODS

All lipids were purchased (Table S1) from Avanti Polar Lipids (Alabaster, AL, USA). Oligonucleotides and primers for RT-qPCR were custom-synthesized (Table S2) by Integrated DNA Technologies (Coralville, IA, USA). The ApoA1 Mimetic Peptide (Table S3) was purchased from Genscript (Piscataway, NJ, USA) with standard TFA removal. TEM samples were prepared on carbon-coated copper grids (400 mesh) obtained from Electron Microscopy Sciences (CF400-Cu; Hatfield, PA, USA) and were stained using Nano-W from Nanoprobes (Yaphank, NY, USA). SMCC (22360), a commercially available DNase I Kit (EN0521), 6× Loading dye (R0611), and Bond-Breaker TCEP Solution (77720) were obtained from ThermoFisher Scientific (Waltham, MA, USA). Hanks' Buffered Salt Solution (HBSS, H8264) and SMCC coupling performed with anhydrous *N,N*-dimethylformamide (DMF, 227056) and *N,N*-diisopropylethylamine (DIPEA, 496219) were purchased from Sigma-Aldrich (St. Louis, MO, USA). All DNA stock solutions and buffers were prepared using Barnstead Nanopure Water System from ThermoFisher Scientific (Waltham, MA, USA) at a resistivity of 18.2 MΩ. Unreacted SMCC was separated from DNA using ethanol precipitation with Koptec USP-grade 200-proof ethanol from Decon Laboratories (V1001; King of Prussia, PA, USA) and sodium acetate (3 M, pH 5.2, molecular biology grade) from Millipore-Sigma (567422; Burlington, MA, USA) and purified using a hydrated P-2 gel from Bio-Rad (1504118; Hercules, CA, USA) or using a NAP-5 Sephadex G-25 column from Cytiva (17085301; Marlborough, MA, USA). DNA separation was performed using a MWCO: 50 kDa Amicon Filter (UFC505024), Blocker of Lipid Transport-1 (SML0059), and Omnipur Agarose (2120-OP) were all purchased from EMD Millipore (Burlington, MA, USA). Quant-iT OliGreen ssDNA Reagent (O7582), DAPI stain: NucBlue Fixed Cell ReadyProbes (R37606), and SYBR Gold Nucleic Acid Gel Stain (S11494) were acquired from Invitrogen (Carlsbad, CA, USA). Cells were cultured in Dulbecco's Modification of Eagle's Medium with L-Glutamine (DMEM, 10-013-CM) using Fetal Bovine Serum (FBS, 35-010-CV) and Penicillin−Streptomycin (30-002-CI) and were detached using Trypsin EDTA (25-053-Cl) from Corning (Tewksbury, MA, USA) and Non-Essential Amino Acids (NEAA, 111450; Gibco; Waltham, MA, USA) when appropriate. qPCR was performed with the following: RNeasy Mini Kit from Qiagen (74106; Hilden, NRW, Germany), High-Capacity cDNA Reverse Transcription Kit from Applied Biosystems (4368814; Foster City, CA, USA), and PerfeCTa SYBR Green FastMix Reaction Mix from QuantaBio (101414-278 [VWR]; Beverly, MA, USA). MTT Cell Proliferation Kit was purchased from Abcam (ab211091; Cambridge, UK).

Synthesis and Characterization of Thiol ND. DMPC and the thiol lipid stocks were combined with chloroform (90:10, 80:20, and 95:5 molar ratios) and placed on a rotary evaporator to dry for 1 h. Cy5-PE was doped in at a molar ratio of 0.15% when necessary for certain experiments. After 1 h, the lipid mixture was placed under a steady stream of nitrogen for 10 min prior to hydrating the lipid film with phosphate buffered saline (PBS, pH 7.4). The mixture was sonicated for 10 min before subjecting it to three freeze−thaw cycles. SUVs were subsequently prepared by passing the mixture 10 times through a 10 mL LIPEX thermobarrel extruder (Evonik Industries, Essen, Germany) using a 80 nm polycarbonate filter. The ApoA1 mimetic peptide (2 mg) was dissolved in nanopure water and added to the SUVs prior to vortexing the mixture for 30 s. The mixture was subjected to three warm−cool cycles alternating between 55 °C and 4 °C for 15 min each as reported in the literature.[30] The thiol-NDs were stored at 4 °C for up to 3 weeks.

DLS and TEM Characterization of Thiol NDs. Prepared NDs were characterized using DLS on a NanoPlus DLS Nano Particle Size and Zeta Potential Analyzer (Micromeritics Instrument Corporation, Norcross, GA, USA) instrument. Sample grids for TEM were prepared by plasmon etching a 400-mesh copper grid for 1 min. A small drop (5 μL) of sample was placed on the grid for 30 s before gently wiping with filter paper so only a small amount of dispersion is left and allowed to dry. One drop of Nano-W was applied to the dried grid for 2 min and was wiped and blotted using the same drying procedure. ND samples were visualized using transmission electron microscopy (TEM) on a Hitachi HT7700 instrument (Chiyoda City, Tokyo, Japan) operating at 80 kV accelerating voltage. TEM images were analyzed using the widely available ImageJ software package.

Addition of Maleimide Group to DNA. SMCC (2 mg) was dissolved in DMF and combined with DIPEA (0.2-fold total volume) and amine-modified DNAzyme (20 nmol) for 1 h at room temperature. Unreacted SMCC was removed through ethanol precipitation. Briefly, cold 200-proof ethanol (800 mL), water (200 mL), and sodium acetate (50 mL of 3 M solution pH 5.2) was added to the sample and frozen at −80 °C to precipitate the DNA. The precipitated solution was centrifuged at maximum speed for 30 min at 4 °C using an Eppendorf 5424R (Hamburg, Germany) refrigerated centrifuge. The supernatant was removed, and the pellet was washed

https://doi.org/10.1021/acs.bioconjchem.1c00505
Bioconjugate Chem. XXXX, XXX, XXX−XXX

twice using copious amounts of 70% ethanol (centrifuging at 4 °C for 10 min at maximum speed in between). The pellet was dried at 37 °C for 15 min and vacuum-dried using an Eppendorf Vacufuge Plus (Hamburg, Germany) for an additional 15 min. Any remaining SMCC, salts, and organic solvent was removed using a P2 gel prior to purifying the product using an AdvanceBio Oligonucleotide (Santa Clara, CA, USA) column and reverse-phase HPLC. DNA strands containing both PS and LNA modifications were purified using a NAP-5 desalting column. The column was washed multiple times with PBS (pH 7.4) prior to adding and collecting the sample (monitored through 260 nm absorbance). Samples were lyophilized overnight before use.

Covalent Linkage of DNA to NDs. Disulfide bonds were reduced in Cy5 containing thiol NDs using 10-fold excess TCEP. TCEP was removed using a centrifugal filtration (MWCO: 50 kDa) and the ND concentration was determined using 650 nm (A_{650}) absorbance to determine Cy5 lipid concentration (Beer's Law, ε = 250,000 M^{-1} cm^{-1}, path length = 0.1 cm), which was used to determine total lipid concentration. Dividing the concentration of lipids (2) by the number of lipids in our ND (1) can give us total concentration (3). Purified Maleimide-DNA was dissolved in PBS (pH 8.5) and combined in 6-fold excess with the reduced thiol NDs. The mixture was agitated gently at 45 °C for 2 h before removing unbound DNA using centrifugal filtration (MWCO: 50 kDa) at 8500 rpm for 10 min and washed four times (or until the supernatant displayed no 260 nm absorbance). Fresh PBS (pH 7.4) was added in between each wash. The number of lipids in a ND was determined as previously reported. The diameter (TEM) provided the radius (r) and enabled us to determine the area (nm^2) and divide it by the area occupied by one DMPC phospholipid (ρ), reported as 0.63 nm^2 (1).

$$\#\ \text{of lipids in single ND} = \frac{\pi r^2}{\rho} \times 2\ \text{leaflets} \tag{1}$$

$$\text{Total [lipid]} = \left(\frac{A_{650}}{(\varepsilon \times 0.1\ \text{cm})}\right) \times \left(\frac{100\%}{0.15\%}\right) \tag{2}$$

$$\text{ND concentration} = \frac{\text{Total ND lipid concentration}}{\#\ \text{of lipids in single ND}} \tag{3}$$

FRET Analysis of ASO-ND Samples. Samples containing 100 nM of fluorescently labeled ASO conjugated to the ND, ASO simply mixed with the ND, and ASO only were prepared in PBS. The fluorometer from Horiba Scientific (Edison, NJ, USA) was blanked using a sample containing PBS or a PBS mixed with ND. The blank subtracted samples were excited at 520 nm and emission spectrum were collected with 20 accumulations, 0.1 integration, and 1-pixel increment. FRET efficiency was calculated (4) by measuring fluorescence emission at 563 nm in the presence of the acceptor and subtracting the value from ASO donor intensity:

$$\text{FRET Efficiency} = \frac{\left[(\text{ASO Donor Intensity}_{563} - \text{Donor Intensity}_{563}\ \text{in the presence of acceptor})\right]}{\left[\text{ASO Donor Intensity}_{563}\right]} \times 100\% \tag{4}$$

Quantification of DNA Density. Commercial OliGreen was used to quantify the DNA density on the ND. Stock concentration of DNA (11 μg/mL) composed of the same sequence strand used to functionalize NDs was prepared at the following concentrations: 0.01, 0.1, 0.2, 0.5, 0.75, and 1 μg/mL in 1× TE buffer, ND, and trypsin, to facilitate structure disassembly, were added to the calibration curve. DNA-ND samples were prepared at various concentrations of 0.2 nM, 0.4 nM, 0.6 nM, and 1.2 nM in 1× TE buffer and trypsin. Assay and calibration curve samples were heated to 85 °C for 10 min and OliGreen reagent was added and mixed thoroughly before measuring the fluorescence intensity (Ex/Em = 485/528 nm) on a Synergy H1 Biotek Plate Reader (Winooski, VT, USA). DNA density values were confirmed by mathematically determining the DNA density by taking the total concentration of DNA on the DNA-ND measured by 260 nm absorbance and dividing it by the ND concentration (3).

Zeta (ζ) Potential Measurement of DNA-ND Samples. DNA-NDs and NDs were loaded into the zeta cells and ζ-potential was measured on the Nano Particle Size and Zeta Potential Analyzer (Micromeritics Instrument Corporation, Norcross, GA, USA) at room temperature.

Gel Electrophoresis. A 1.5% agarose gel was prepared using in-gel staining with SYBR Gold (10,000-fold dilution). Samples (5 μL) containing DNA only, fluorescently labeled ND only, and fluorescently labeled DNA-ND were mixed with 6× loading dye (5 μL), and samples were loaded onto the gel. The gel was run at 85 V for 1.5 h on a Bio-Rad PowerPac Basic Electrophoresis Supply (Hercules, CA, USA) and visualized using an Amersham Typhoon laser scanner (Cytiva, Marlborough, MA, USA).

DNAzyme Kinetics and Nuclease Degradation Assay. The DNAzyme-ND was diluted to 10 nM (DNA concentration) in HEPES buffer (10 mM HEPES, 150 mM NaCl, pH 7.4), and the solution was directly transferred to a 96-well plate (100 μL). The DNAzyme substrate was prepared at 100 nM using HEPES buffer supplemented with magnesium (10 mM HEPES, 150 mM NaCl, 2 mM $MgCl_2$, pH 7.4) and added to the well-plate containing the DNAzyme samples (total volume = 200 μL). The FAM fluorescence intensity was immediately monitored for 4 h with the plate reader. The DNA-ND samples and soluble (free) DNAzyme (1 μM) were incubated with 1 U of DNase I of the supplied reaction buffer (final concentrations: 10 mM Tris-HCl, 2.5 mM $MgCl_2$, and 0.1 mM $CaCl_2$) at 37 °C for 2 h. Thereafter, the DNase I was quenched using the supplied EDTA (5 mM) and inactivated at 65 °C for 10 min, as per the accompanying protocol. The samples were transferred to a 96 well plate and combined with the DNAzyme substrate solution (10 mM HEPES, 150 mM NaCl, 10 μM DNAzyme substrate, 4 mM $MgCl_2$, pH = 7.4), and FAM fluorescence intensity was immediately monitored for 2.5 h using the plate reader.

Cell Culture. HeLa cells (ATCC), U373 cells (Sigma-Aldrich), and PLC/PRF/5 (ATCC) cells were cultured in DMEM with 10% FBS and penicillin (100 U/mL) and streptomycin (100 mg/mL). NEAA (1%, 100×) was supplemented to the media of U373 cells and PLC/PRF/5. Cells were maintained at 37 °C under a humidified CO_2 atmosphere (5%).

https://doi.org/10.1021/acs.bioconjchem.1c00505
Bioconjugate Chem. XXXX, XXX, XXX−XXX

Confocal Microscopy of HeLa Cells. HeLa cells were plated at a density of 1×10^4 cells/well in a Nunc 96 well black optical plate (265300, ThermoFisher, Waltham, MA, USA) the day before the experiment. Fluorescently labeled ASO-ND (100 nM) were incubated with cells for 3, 12, or 24 h prior to fixing cells with 4% paraformaldehyde. Cells were washed three times using PBS (pH 7.4) and stained using DAPI. Cells were imaged on a Nikon Ti2 Eclipse confocal microscope (Minato City, Tokyo, Japan) with a 60× oil objective, Nikon Elements, perfect focus, and a C2 laser scanning system. Z-stacks were collected with a 0.15 μm step size. Cell images were analyzed using ImageJ and Pearson's Coefficient using the Just Another Colocalization ImageJ plugin.

Dose- and Time-Dependent Uptake Measurements Using Flow Cytometry. HeLa, U373, and PLC/PRF/5 cells were plated at a density of 8×10^4 cells/well in tissue culture-treated 12-well plates the day before experiment. Fluorescently labeled ASO-ND (ND concentrations: 5 nM, 25 nM, 50 nM, 100 nM) for 4, 12, or 24 h before cells were washed with sterile PBS (pH 7.4) once before adding trypsin and collecting cells for flow. Trypsinized cells were washed with HBSS twice, prior to resuspending the cells in fresh HBSS for flow cytometry assessment on a Beckman Coulter Cytoflex (Pasadena, CA, USA) to measure cell associated Cy5 fluorescence intensity. Histograms were prepared using FlowJo software (FlowJo LLC, Ashland, OR, USA).

SRB1 Mediated Uptake of ASO-NDs. HeLa, U373, and PLC/PRF/5 cells were plated at a density of 8×10^4 cells/well in tissue culture-treated 12-well plates the day before experiment. Cells were treated with BLT-1 (50 μM) in serum-free DMEM for 1 h. Anti-HIF-1-α ASO-ND (15 nM) was added and incubated with cells for 2 h, prior to washing cells and collecting and analyzing cells for flow in the same procedure as described above. Fluorescence intensity was compared against untreated cells containing ND or ASO-ND.

RT-qPCR to Assess HIF-1-α Levels after EZN-2968 ASO-ND Treatment *in Vitro*. HeLa, U373, and PLC/PRF/5 cells were plated at a density of 5×10^4 cells/well in tissue culture-treated 24-well plates the day before the experiment. Anti-HIF-1-α ASO-ND, soluble anti-HIF-1-α, Scrambled-ND, and NDs were incubated with cells for 24 h. Cells were lysed using QIAZOL and total RNA was collected as per the accompanied QIAGEN extraction kit procedure. RNA was reverse-transcribed as per the recommended protocol for the High-Capacity cDNA Reverse Transcription Kit using a T100 Thermal Cycler (Bio-Rad, Hercules, CA, USA). HIF-1-α mRNA levels were quantified using quantitative real-time PCR (RT-qPCR) using PerfeCTa SYBR Green FastMix and 50 μM custom primers (Table S2) and a Roche Lightcycler 96 (Basel, Switzerland) instrument. Relative quantification of mRNA levels was determined using the $\Delta\Delta C_t$ method with 18S mRNA levels for an internal control.

Comparing Dose-Dependent Uptake of anti-HIF-1-α ASO and anti-HIF-1-α ASO-NDs. HeLa cells were plated at a density of 8×10^4 cells/well in tissue-culture treated 12-well plates the day before the experiment. Anti-HIF-1-α ASO-NDs and soluble anti-HIF-1-α ASO were incubated with cells for 24 h prior to washing cells and collecting and analyzing cells for flow in the same procedure as described above. Fluorescence intensity was compared of the soluble anti-HIF-1-α against the soluble anti-HIF-1-α ASO-ND.

MTT Assay to Assess Cell Viability. HeLa cells were plated at a density of 1×10^4 cells/well in a tissue-culture treated 96-well plates the day before the experiment. The following day, the media was exchanged for fresh media, and anti-HIF-1-α-ND, soluble anti-HIF-1-α, scrambled-ND, and NDs were incubated with cells for 24 or 48 h. The cells were rinsed with fresh media prior to adding 50 μL of phenol red-free and serum-free DMEM and 50 μL of prewarmed (37 °C) MTT solution. The cells were placed in the incubator at 37 °C for 3 h before adding 150 μL of prewarmed MTT solvent. Subsequently, the plate was covered in foil and placed on a shaker for 15 min before reading the optical density at 590 nm on a plate reader. Cell viability was assessed from determining the cytotoxicity and normalizing to the untreated control (at 100%).

■ ASSOCIATED CONTENT

Supporting Information

The Supporting Information is available free of charge at https://pubs.acs.org/doi/10.1021/acs.bioconjchem.1c00505.

TEM and DNA density using click chemistry; TEM images of NDs prepared with different ratios of thiol lipids; DLS stability data of DNA-NDs; plot of catalytic activity of the DNA-NDs against a mock substrate; confocal microscopy and Z-stack analysis of ASO-NDs at various time points over 24 h; quantifying ND uptake into cells using flow cytometry; RT-qPCR measurement for SRB1 expression in HeLa, U373, and PLC/PRF/5 cells; role of SRB1 in the uptake of ND scaffold; quantitative mean flow cytometry plots after treating cells with SRB1 inhibitor; activity factor comparing the activity of ASO-ND vs ASO only on a per molecule basis; MTT assay for cell viability in HeLa cells (PDF)

■ AUTHOR INFORMATION

Corresponding Author

Khalid Salaita − *Department of Chemistry, Emory University, Atlanta, Georgia 30332, United States;* orcid.org/0000-0003-4138-3477; Email: k.salaita@emory.edu

Authors

Radhika Sharma − *Department of Chemistry, Emory University, Atlanta, Georgia 30332, United States*

Yixiao Dong − *Department of Chemistry, Emory University, Atlanta, Georgia 30332, United States;* orcid.org/0000-0001-8943-9842

Yuesong Hu − *Department of Chemistry, Emory University, Atlanta, Georgia 30332, United States*

Victor Pui-Yan Ma − *Department of Chemistry, Emory University, Atlanta, Georgia 30332, United States;* orcid.org/0000-0002-5951-0297

Complete contact information is available at: https://pubs.acs.org/10.1021/acs.bioconjchem.1c00505

Author Contributions

R.S. and K.S. designed the experiments. R.S. performed all synthesis, characterization, confocal microscopy, flow cytometry, RT-qPCR, and all data analysis. Y.D. prepared samples and performed TEM. Y. H. and V. P.-Y. Ma. assisted in initial design strategies and approach.

Funding

K. S. acknowledges generous support from the National Institutes of Health (R01HL142866). V. P.-Y. Ma. is

https://doi.org/10.1021/acs.bioconjchem.1c00505
Bioconjugate Chem. XXXX, XXX, XXX−XXX

supported by the National Cancer Institute Predoctoral to Postdoctoral Fellow Transition Award (K00CA223074).

Notes

The authors declare no competing financial interest.

■ ACKNOWLEDGMENTS

The authors would like to thank Hiroaki Ogasawara for useful advice all throughout this study. Some illustrations were based on Biorender icons.

■ REFERENCES

(1) Xiong, H.; Veedu, R. N.; Diermeier, S. D. Recent Advances in Oligonucleotide Therapeutics in Oncology. *Int. J. Mol. Sci.* **2021**, *22* (7), 3295.

(2) Gagliardi, M.; Ashizawa, A. T. The Challenges and Strategies of Antisense Oligonucleotide Drug Delivery. *Biomedicines* **2021**, *9* (4), 433.

(3) Deleavey, G. F.; Damha, M. J. Designing Chemically Modified Oligonucleotides for Targeted Gene Silencing. *Chemistry & Biology* **2012**, *19* (8), 937−954.

(4) Roberts, T. C.; Langer, R.; Wood, M. J. A. Advances in oligonucleotide drug delivery. *Nat. Rev. Drug Discovery* **2020**, *19* (10), 673−694.

(5) Juliano, R. L. The delivery of therapeutic oligonucleotides. *Nucleic Acids Res.* **2016**, *44* (14), 6518−48.

(6) Khvorova, A.; Watts, J. K. The chemical evolution of oligonucleotide therapies of clinical utility. *Nat. Biotechnol.* **2017**, *35* (3), 238−248.

(7) Beltinger, C.; Saragovi, H. U.; Smith, R. M.; LeSauteur, L.; Shah, N.; DeDionisio, L.; Christensen, L.; Raible, A.; Jarett, L.; Gewirtz, A. M. Binding, uptake, and intracellular trafficking of phosphorothioate-modified oligodeoxynucleotides. *J. Clin. Invest.* **1995**, *95* (4), 1814−1823.

(8) Eckstein, F. Phosphorothioates, Essential Components of Therapeutic Oligonucleotides. *Nucleic Acid Therapeutics* **2014**, *24* (6), 374−387.

(9) Crooke, S. T.; Vickers, T. A.; Liang, X. H. Phosphorothioate modified oligonucleotide-protein interactions. *Nucleic Acids Res.* **2020**, *48* (10), 5235−5253.

(10) Dowdy, S. F. Overcoming cellular barriers for RNA therapeutics. *Nat. Biotechnol.* **2017**, *35* (3), 222−229.

(11) Pei, D.; Buyanova, M. Overcoming Endosomal Entrapment in Drug Delivery. *Bioconjugate Chem.* **2019**, *30* (2), 273−283.

(12) Frazier, K. S. Antisense Oligonucleotide Therapies: The Promise and the Challenges from a Toxicologic Pathologist's Perspective. *Toxicologic Pathology* **2015**, *43* (1), 78−89.

(13) Cutler, J. I.; Auyeung, E.; Mirkin, C. A. Spherical Nucleic Acids. *J. Am. Chem. Soc.* **2012**, *134* (3), 1376−1391.

(14) Yehl, K.; Joshi, J. P.; Greene, B. L.; Dyer, R. B.; Nahta, R.; Salaita, K. Catalytic Deoxyribozyme-Modified Nanoparticles for RNAi-Independent Gene Regulation. *ACS Nano* **2012**, *6* (10), 9150−9157.

(15) McMahon, K. M.; Mutharasan, R. K.; Tripathy, S.; Veliceasa, D.; Bobeica, M.; Shumaker, D. K.; Luthi, A. J.; Helfand, B. T.; Ardehali, H.; Mirkin, C. A.; Volpert, O.; Thaxton, C. S. Biomimetic High Density Lipoprotein Nanoparticles For Nucleic Acid Delivery. *Nano Lett.* **2011**, *11* (3), 1208−1214.

(16) Liu, B.; Wu, P.; Huang, Z.; Ma, L.; Liu, J. Bromide as a Robust Backfiller on Gold for Precise Control of DNA Conformation and High Stability of Spherical Nucleic Acids. *J. Am. Chem. Soc.* **2018**, *140* (13), 4499−4502.

(17) Mokhtarzadeh, A.; Vahidnezhad, H.; Youssefian, L.; Mosafer, J.; Baradaran, B.; Uitto, J. Applications of Spherical Nucleic Acid Nanoparticles as Delivery Systems. *Trends in Molecular Medicine* **2019**, *25* (12), 1066−1079.

(18) Mitchell, M. J.; Billingsley, M. M.; Haley, R. M.; Wechsler, M. E.; Peppas, N. A.; Langer, R. Engineering precision nanoparticles for drug delivery. *Nat. Rev. Drug Discovery* **2021**, *20* (2), 101−124.

(19) Zannis, V. I.; Chroni, A.; Krieger, M. Role of apoA-I, ABCA1, LCAT, and SR-BI in the biogenesis of HDL. *Journal of Molecular Medicine* **2006**, *84* (4), 276−294.

(20) Patel, H.; Ding, B.; Ernst, K.; Shen, L.; Yuan, W.; Tang, J.; Drake, L. R.; Kang, J.; Li, Y.; Chen, Z.; Schwendeman, A. Characterization of apolipoprotein A-I peptide phospholipid interaction and its effect on HDL nanodisc assembly. *Int. J. Nanomedicine* **2019**, *14*, 3069−3086.

(21) Kuai, R.; Ochyl, L. J.; Bahjat, K. S.; Schwendeman, A.; Moon, J. J. Designer vaccine nanodiscs for personalized cancer immunotherapy. *Nat. Mater.* **2017**, *16* (4), 489−496.

(22) Ding, Y.; Wang, W.; Feng, M.; Wang, Y.; Zhou, J.; Ding, X.; Zhou, X.; Liu, C.; Wang, R.; Zhang, Q. A biomimetic nanovector-mediated targeted cholesterol-conjugated siRNA delivery for tumor gene therapy. *Biomaterials* **2012**, *33* (34), 8893−8905.

(23) Agarwal, R.; Singh, V.; Jurney, P.; Shi, L.; Sreenivasan, S. V.; Roy, K. Mammalian cells preferentially internalize hydrogel nanodiscs over nanorods and use shape-specific uptake mechanisms. *Proc. Natl. Acad. Sci. U. S. A.* **2013**, *110* (43), 17247.

(24) Wolfrum, C.; Shi, S.; Jayaprakash, K. N.; Jayaraman, M.; Wang, G.; Pandey, R. K.; Rajeev, K. G.; Nakayama, T.; Charrise, K.; Ndungo, E. M.; Zimmermann, T.; Koteliansky, V.; Manoharan, M.; Stoffel, M. Mechanisms and optimization of in vivo delivery of lipophilic siRNAs. *Nat. Biotechnol.* **2007**, *25* (10), 1149−1157.

(25) Cruz, W.; Huang, H.; Barber, B.; Pasini, E.; Ding, L.; Zheng, G.; Chen, J.; Bhat, M. Lipoprotein-Like Nanoparticle Carrying Small Interfering RNA Against Spalt-Like Transcription Factor 4 Effectively Targets Hepatocellular Carcinoma Cells and Decreases Tumor Burden. *Hepatology Communications* **2020**, *4* (5), 769−782.

(26) Kuwahara, H.; Nishina, K.; Yoshida, K.; Nishina, T.; Yamamoto, M.; Saito, Y.; Piao, W.; Yoshida, M.; Mizusawa, H.; Yokota, T. Efficient In Vivo Delivery of siRNA Into Brain Capillary Endothelial Cells Along With Endogenous Lipoprotein. *Molecular Therapy* **2011**, *19* (12), 2213−2221.

(27) Uno, Y.; Piao, W.; Miyata, K.; Nishina, K.; Mizusawa, H.; Yokota, T. High-Density Lipoprotein Facilitates In Vivo Delivery of α-Tocopherol−Conjugated Short-Interfering RNA to the Brain. *Hum. Gene Ther.* **2011**, *22* (6), 711−719.

(28) McMahon, K. M.; Plebanek, M. P.; Thaxton, C. S. Properties of Native High-Density Lipoproteins Inspire Synthesis of Actively Targeted In Vivo siRNA Delivery Vehicles. *Adv. Funct. Mater.* **2016**, *26* (43), 7824−7835.

(29) McMahon, K. M.; Thaxton, C. S. High-density lipoproteins for the systemic delivery of short interfering RNA. *Expert Opinion on Drug Delivery* **2014**, *11* (2), 231−247.

(30) Kadiyala, P.; Li, D.; Nuñez, F. M.; Altshuler, D.; Doherty, R.; Kuai, R.; Yu, M.; Kamran, N.; Edwards, M.; Moon, J. J.; Lowenstein, P. R.; Castro, M. G.; Schwendeman, A. High-Density Lipoprotein-Mimicking Nanodiscs for Chemo-immunotherapy against Glioblastoma Multiforme. *ACS Nano* **2019**, *13* (2), 1365−1384.

(31) Tahmasbi Rad, A.; Malik, S.; Yang, L.; Oberoi-Khanuja, T. K.; Nieh, M.-P.; Bahal, R. A universal discoidal nanoplatform for the intracellular delivery of PNAs. *Nanoscale* **2019**, *11* (26), 12517−12529.

(32) Wang, J.; Calvert, A. E.; Kaplan, N.; McMahon, K. M.; Yang, W.; Lu, K. Q.; Peng, H.; Thaxton, C. S.; Lavker, R. M. HDL Nanoparticles Have Wound Healing and Anti-Inflammatory Properties and Can Topically Deliver miRNAs. *Advanced Therapeutics* **2020**, *3* (12), 2000138.

(33) Tripathy, S.; Vinokour, E.; McMahon, K. M.; Volpert, O. V.; Thaxton, C. S. High Density Lipoprotein Nanoparticles Deliver RNAi to Endothelial Cells to Inhibit Angiogenesis. *Part Part Syst. Charact* **2014**, *31* (11), 1141−1150.

(34) Ghosh, M.; Ren, G.; Simonsen, J. B.; Ryan, R. O. Cationic lipid nanodisks as an siRNA delivery vehicle. *Biochem Cell Biol.* **2014**, *92* (3), 200−205.

https://doi.org/10.1021/acs.bioconjchem.1c00505
Bioconjugate Chem. XXXX, XXX, XXX−XXX

(35) Shahzad, M. M. K.; Mangala, L. S.; Han, H. D.; Lu, C.; Bottsford-Miller, J.; Nishimura, M.; Mora, E. M.; Lee, J.-W.; Stone, R. L.; Pecot, C. V.; Thanapprapasr, D.; Roh, J.-W.; Gaur, P.; Nair, M. P.; Park, Y.-Y.; Sabnis, N.; Deavers, M. T.; Lee, J.-S.; Ellis, L. M.; Lopez-Berestein, G.; McConathy, W. J.; Prokai, L.; Lacko, A. G.; Sood, A. K. Targeted Delivery of Small Interfering RNA Using Reconstituted High-Density Lipoprotein Nanoparticles. *Neoplasia* **2011**, *13* (4), 309−IN8.
(36) Meckes, B.; Banga, R. J.; Nguyen, S. T.; Mirkin, C. A. Enhancing the Stability and Immunomodulatory Activity of Liposomal Spherical Nucleic Acids through Lipid-Tail DNA Modifications. *Small* **2018**, *14* (5), 1702909.
(37) Yang, M.; Jin, H.; Chen, J.; Ding, L.; Ng, K. K.; Lin, Q.; Lovell, J. F.; Zhang, Z.; Zheng, G. Efficient Cytosolic Delivery of siRNA Using HDL-Mimicking Nanoparticles. *Small* **2011**, *7* (5), 568−573.
(38) Nakayama, T.; Butler, J. S.; Sehgal, A.; Severgnini, M.; Racie, T.; Sharman, J.; Ding, F.; Morskaya, S. S.; Brodsky, J.; Tchangov, L.; Kosovrasti, V.; Meys, M.; Nechev, L.; Wang, G.; Peng, C. G.; Fang, Y.; Maier, M.; Rajeev, K. G.; Li, R.; Hettinger, J.; Barros, S.; Clausen, V.; Zhang, X.; Wang, Q.; Hutabarat, R.; Dokholyan, N. V.; Wolfrum, C.; Manoharan, M.; Kotelianski, V.; Stoffel, M.; Sah, D. W. Y. Harnessing a Physiologic Mechanism for siRNA Delivery With Mimetic Lipoprotein Particles. *Molecular Therapy* **2012**, *20* (8), 1582−1589.
(39) Jeong, W.; Rapisarda, A.; Park, S. R.; Kinders, R. J.; Chen, A.; Melillo, G.; Turkbey, B.; Steinberg, S. M.; Choyke, P.; Doroshow, J. H.; Kummar, S. Pilot trial of EZN-2968, an antisense oligonucleotide inhibitor of hypoxia-inducible factor-1 alpha (HIF-1α), in patients with refractory solid tumors. *Cancer Chemother Pharmacol* **2014**, *73* (2), 343−348.
(40) Patnaik, A.; Chiorean, E. G.; Tolcher, A.; Papadopoulos, K.; Beeram, M.; Kee, D.; Waddell, M.; Gilles, E.; Buchbinder, A. EZN-2968, a novel hypoxia-inducible factor-1α (HIF-1α) messenger ribonucleic acid (mRNA) antagonist: Results of a phase I, pharmacokinetic (PK), dose-escalation study of daily administration in patients (pts) with advanced malignancies. *Journal of Clinical Oncology* **2009**, *27* (15), 2564−2564.
(41) Imura, T.; Tsukui, Y.; Taira, T.; Aburai, K.; Sakai, K.; Sakai, H.; Abe, M.; Kitamoto, D. Surfactant-like Properties of an Amphiphilic α-Helical Peptide Leading to Lipid Nanodisc Formation. *Langmuir* **2014**, *30* (16), 4752−4759.
(42) Denisov, I. G.; Sligar, S. G. Nanodiscs for structural and functional studies of membrane proteins. *Nature Structural & Molecular Biology* **2016**, *23* (6), 481−486.
(43) Kariyazono, H.; Nadai, R.; Miyajima, R.; Takechi-Haraya, Y.; Baba, T.; Shigenaga, A.; Okuhira, K.; Otaka, A.; Saito, H. Formation of stable nanodiscs by bihelical apolipoprotein A-I mimetic peptide. *Journal of Peptide Science* **2016**, *22* (2), 116−122.
(44) Siuda, I.; Tieleman, D. P. Molecular Models of Nanodiscs. *J. Chem. Theory Comput.* **2015**, *11* (10), 4923−4932.
(45) Bengtsen, T.; Holm, V. L.; Kjølbye, L. R.; Midtgaard, S. R.; Johansen, N. T.; Tesei, G.; Bottaro, S.; Schiøtt, B.; Arleth, L.; Lindorff-Larsen, K. Structure and dynamics of a nanodisc by integrating NMR, SAXS and SANS experiments with molecular dynamics simulations. *Elife* **2020**, *9*, e56518.
(46) Zhang, L.; Song, J.; Cavigiolio, G.; Ishida, B. Y.; Zhang, S.; Kane, J. P.; Weisgraber, K. H.; Oda, M. N.; Rye, K.-A.; Pownall, H. J.; Ren, G. Morphology and structure of lipoproteins revealed by an optimized negative-staining protocol of electron microscopy [S]. *J. Lipid Res.* **2011**, *52* (1), 175−184.
(47) Santoro, S. W.; Joyce, G. F. A general purpose RNA-cleaving DNA enzyme. *Proc. Natl. Acad. Sci. U. S. A.* **1997**, *94* (9), 4262.
(48) Wang, Y.; Nguyen, K.; Spitale, R. C.; Chaput, J. C. A biologically stable DNAzyme that efficiently silences gene expression in cells. *Nat. Chem.* **2021**, *13* (4), 319−326.
(49) Gavitt, T. D.; Hartmann, A. K.; Sawant, S. S.; Mara, A. B.; Szczepanek, S. M.; Rouge, J. L. A GATA3 Targeting Nucleic Acid Nanocapsule for In Vivo Gene Regulation in Asthma. *ACS Nano* **2021**, *15* (7), 11192−11201.
(50) Petree, J. R.; Yehl, K.; Galior, K.; Glazier, R.; Deal, B.; Salaita, K. Site-Selective RNA Splicing Nanozyme: DNAzyme and RtcB Conjugates on a Gold Nanoparticle. *ACS Chem. Biol.* **2018**, *13* (1), 215−224.
(51) Somasuntharam, I.; Yehl, K.; Carroll, S. L.; Maxwell, J. T.; Martinez, M. D.; Che, P.-L.; Brown, M. E.; Salaita, K.; Davis, M. E. Knockdown of TNF-α by DNAzyme gold nanoparticles as an anti-inflammatory therapy for myocardial infarction. *Biomaterials* **2016**, *83*, 12−22.
(52) Zhang, J.; Ma, R.; Blanchard, A.; Petree, J.; Jo, H.; Salaita, K. Conditional Deoxyribozyme−Nanoparticle Conjugates for miRNA-Triggered Gene Regulation. *ACS Appl. Mater. Interfaces* **2020**, *12* (34), 37851−37861.
(53) Hartmann, A. K.; Cairns-Gibson, D. F.; Santiana, J. J.; Tolentino, M. Q.; Barber, H. M.; Rouge, J. L. Enzymatically Ligated DNA−Surfactants: Unmasking Hydrophobically Modified DNA for Intracellular Gene Regulation. *ChemBioChem.* **2018**, *19* (16), 1734−1739.
(54) Zhang, Z.; Cao, W.; Jin, H.; Lovell, J. F.; Yang, M.; Ding, L.; Chen, J.; Corbin, I.; Luo, Q.; Zheng, G. Biomimetic Nanocarrier for Direct Cytosolic Drug Delivery. *Angew. Chem., Int. Ed.* **2009**, *48* (48), 9171−9175.
(55) Crooke, S. T.; Wang, S.; Vickers, T. A.; Shen, W.; Liang, X.-h. Cellular uptake and trafficking of antisense oligonucleotides. *Nat. Biotechnol.* **2017**, *35* (3), 230−237.
(56) Huo, S.; Li, H.; Boersma, A. J.; Herrmann, A. DNA Nanotechnology Enters Cell Membranes. *Advanced Science* **2019**, *6* (10), 1900043.
(57) Kuai, R.; Li, D.; Chen, Y. E.; Moon, J. J.; Schwendeman, A. High-Density Lipoproteins: Nature's Multifunctional Nanoparticles. *ACS Nano* **2016**, *10* (3), 3015−3041.
(58) Acton, S.; Rigotti, A.; Landschulz, K. T.; Xu, S.; Hobbs, H. H.; Krieger, M. Identification of scavenger receptor SR-BI as a high density lipoprotein receptor. *Science* **1996**, *271* (5248), 518−20.
(59) Lee, J.-W.; Bae, S.-H.; Jeong, J.-W.; Kim, S.-H.; Kim, K.-W. Hypoxia-inducible factor (HIF-1)α: its protein stability and biological functions. *Experimental & Molecular Medicine* **2004**, *36* (1), 1−12.
(60) Ryan, H. E.; Lo, J.; Johnson, R. S. HIF-1α is required for solid tumor formation and embryonic vascularization. *EMBO Journal* **1998**, *17* (11), 3005−3015.
(61) Hong, W. X.; Hu, M. S.; Esquivel, M.; Liang, G. Y.; Rennert, R. C.; McArdle, A.; Paik, K. J.; Duscher, D.; Gurtner, G. C.; Lorenz, H. P.; Longaker, M. T. The Role of Hypoxia-Inducible Factor in Wound Healing. *Adv. Wound Care (New Rochelle)* **2014**, *3* (5), 390−399.
(62) Koh, M. Y.; Spivak-Kroizman, T.; Venturini, S.; Welsh, S.; Williams, R. R.; Kirkpatrick, D. L.; Powis, G. Molecular mechanisms for the activity of PX-478, an antitumor inhibitor of the hypoxia-inducible factor-1α. *Molecular Cancer Therapeutics* **2008**, *7* (1), 90.
(63) Onnis, B.; Rapisarda, A.; Melillo, G. Development of HIF-1 inhibitors for cancer therapy. *Journal of Cellular and Molecular Medicine* **2009**, *13* (9a), 2780−2786.
(64) Juliano, R. L.; Ming, X.; Carver, K.; Laing, B. Cellular Uptake and Intracellular Trafficking of Oligonucleotides: Implications for Oligonucleotide Pharmacology. *Nucleic Acid Therapeutics* **2014**, *24* (2), 101−113.
(65) Gao, F.; Chattopadhyay, A.; Navab, M.; Grijalva, V.; Su, F.; Fogelman, A. M.; Reddy, S. T.; Farias-Eisner, R. Apolipoprotein A-I Mimetic Peptides Inhibit Expression and Activity of Hypoxia-Inducible Factor-1α in Human Ovarian Cancer Cell Lines and a Mouse Ovarian Cancer Model. *Journal of Pharmacology and Experimental Therapeutics* **2012**, *342* (2), 255.
(66) Weidemann, A.; Johnson, R. S. Biology of HIF-1α. *Cell Death & Differentiation* **2008**, *15* (4), 621−627.
(67) Zhang, J.; Sharma, R.; Ryu, K.; Shen, P.; Salaita, K.; Jo, H. Conditional Antisense Oligonucleotide Triggered by miRNA. *ACS Chem. Biol.* **2021**, *16*, 2255.
(68) Ben-Aicha, S.; Escate, R.; Casaní, L.; Padró, T.; Peña, E.; Arderiu, G.; Mendieta, G.; Badimón, L.; Vilahur, G. High-density lipoprotein remodelled in hypercholesterolaemic blood induce

https://doi.org/10.1021/acs.bioconjchem.1c00505
Bioconjugate Chem. XXXX, XXX, XXX−XXX

epigenetically driven down-regulation of endothelial HIF-1α expression in a preclinical animal model. *Cardiovasc. Res.* **2020**, *116* (7), 1288−1299.

https://doi.org/10.1021/acs.bioconjchem.1c00505
Bioconjugate Chem. XXXX, XXX, XXX−XXX